Energy Conversion and Management: X 28 (2025) 101236

Contents lists available at ScienceDirect

Energy Conversion and Management: X

journal homepage: www.sciencedirect.com/journal/energy-conversion-and-management-x

Control concept for solid oxide electrolysis reactors to promote highly transient operation in modular plants

René Lorenz *, Jan Hollmann, Marius Tomberg, Marc P. Heddrich, S. Asif Ansar

German Aerospace Center (DLR), Institute of Engineering Thermodynamics, Pfaffenwaldring 38-40, Stuttgart, 70569, Germany

ARTICLE INFO

Dataset link: http://uni-oldenburg.de/fileadmin/user_upload/physik/ag/twist/Forschung/Daten/AnvariEtAl2016_ExampleData_WindPowerAndIrradianceData.zip

Keywords:
Solid Oxide Electrolysis Cells (SOEC)
Dynamic operation
Thermal management
Limiting temperature gradients
Renewable power to hydrogen
Modular SOEC plants

ABSTRACT

Solid Oxide Electrolysis Cells (SOECs) offer the lowest specific electrical energy demand among electrolysis technologies, making them highly suitable for large-scale hydrogen production, where electricity accounts for 70 %–85 % of the levelized cost of hydrogen. To comply with guarantees of origin for green hydrogen, SOEC systems must operate reliably in power-following mode with fluctuating renewable energy sources (RES). However, transient operation induces thermal gradients within SOEC stacks, accelerating degradation and increasing the risk of premature failure.

This study proposes a dynamic control concept that enables rapid power modulation with limited thermal stress, based on an experimentally validated multi-stack SOEC reactor model. A large-scale SOEC plant is considered, consisting of multiple modules, each comprising a multi-stack reactor and independent balance-of-plant components. The module-level power control employs a PI controller, augmented with model-based current slew-rate limit correlations and feed-forward step changes between hot standby and thermoneutral operation. For a moderate thermal gradient limit of $\pm 5\,\mathrm{K\,min^{-1}}$, optimised control parameters enables transitions from hot standby to 80 % nominal power in 35 s and to 100 % in 3 min – approximately six times faster than conventional linear current ramps. The control concept is further applied to a modular SOEC plant under a real wind park power profile. Two key factors influencing power-following capability are identified: the number of modules and the lower power limit of an individual module's operating range ($P_{\mathrm{mod,low}}$). The proposed control concept improves power-following capability by reducing power mismatch by 45 % and significantly decreases the required module count, enhancing both system efficiency and scalability.

1. Introduction

Renewable energy-powered electrolysis is a promising path to defossilise the energy supply for industrial, transportation and energy sectors. The produced hydrogen or syngas (H_2 + CO) can be stored and later converted back into electricity or utilised as a feedstock for energy-intensive processes that are difficult to electrify, such as heavy industry, long-distance air and sea transportation, and chemical industry [1,2]. Among the available technologies, high-temperature electrolysis based on Solid Oxide Cell (SOC) reactors achieves highest efficiencies, particularly when heat integration with other processes can provide the energy for steam production. However, operating Solid Oxide Electrolysis Cells (SOEC) with fluctuating renewable energy sources, such as wind and solar power, requires strategies to manage variable power availability. Large battery storage systems are expensive and should be minimised, necessitating transient operation of SOC reactors to align with the variable power supply. This poses a challenge since SOECs are sensitive to high thermal gradients, which can arise during rapid changes in the operating point (OP). The electrolysis reaction is endothermic, consuming heat, while Joule heating generates heat as current flows through the cells. The heat generation rate is a function of cell resistance and current squared ($\dot{Q} = I^2 R$) [3]. At low currents, the endothermic effect dominates (endothermic operation), whereas at higher currents, Joule heating prevails (exothermic operation). Heat generation and consumption are balanced at thermoneutral operation, which corresponds to thermoneutral voltage:

$$U_{\mathrm{tn}}(T) = \Delta^{\mathrm{R}} H_{\mathrm{m}}(T)/zF \ , \tag{1}$$

where $\Delta^{\mathrm{R}} H_{\mathrm{m}}$ is the molar reaction enthalpy, z is the number of transferred electrons (steam electrolysis: z=2), and F is Faraday's constant. In real systems, heat losses to the surroundings contribute to the overall heat consumption. To maintain thermal equilibrium and isothermal conditions, a higher voltage is required to compensate for the additional heat dissipation: $U_{\mathrm{isothermal}}(T) > U_{\mathrm{tn}}(T)$. Isothermal operation in real systems is defined as the point where the gas outlet temperature

* Corresponding author.
E-mail address: Rene.Lorenz@dlr.de (R. Lorenz).

https://doi.org/10.1016/j.ecmx.2025.101236
Received 5 May 2025; Received in revised form 19 August 2025; Accepted 28 August 2025
Available online 3 September 2025

Nomenclature

Abbreviations

ASR	Area specific resistance
LHV	Lower heating value
EC	Electrolysis mode
FC	Fuell cell mode
OP	Operating Point
PI	Proportional–integral (controller)
RMSE	Root Mean Square Error
SOC	Solid Oxide Cell
SOEC	Solid Oxide Electrolysis Cell

Greek symbols

Δ	Difference
η	Efficiency

Latin symbols

$\dot{m}$	Mass flow rate
$\dot{n}$	Molar flow rate
$\dot{Q}$	Heat flow rate
A	Area
C	Constant
F	Faraday's constant
f	Factor
H	Enthalpy
I	Current
i	Current density
M	Molar mass
N	Number of modules
P	Power
p	Pressure
RC	Reactant conversion
T	Temperature
t	Time
U	Voltage
x	Length
z	Number of transferred electrons

Sub- and superscripts

act	actual value
act	in active operation (N_{act})
BoP	balance of plant
el	electric
high	higher limit
id	ideal
j	enumeration item
k	enumeration item
low	lower limit
m	molar
max	maximum
min	minimum
mod	module
nom	nominal
PE	power electronics
pl	plant
R	reaction
set	setpoint value
stdby	standby
TC	thermocouple
tn	thermoneutral
wind	wind park

matches the reactor's inlet temperature, i.e., $T_{\text{gas,in}} = T_{\text{gas,out}}$. Temperature differences between endothermic, isothermal, and exothermic operation can be significant. Rapid changes of the operating point can result in large temperature gradients, risking increased degradation or even damage to the stack. Therefore, effective operating and control strategies are critical for safe and efficient operation under transient conditions. Key control parameters include fuel and air mass flows, inlet temperatures, and reactant conversion (RC), which relates fuel mass flow and composition to current density. Unlike fuel cell operation, electrolysis does not require air/oxygen supply. Nevertheless, most state-of-the-art multi-stack SOEC reactors use air to dilute and flush out the produced oxygen and for temperature control.

Several studies have proposed air mass flow as the primary parameter for temperature control during dynamic operation [4–7]. While air flow rates can remain low near thermoneutral operation, strongly endothermic or exothermic conditions require high air flow rates, which negatively affect system efficiency. Additionally, the large variations in air mass flow has to be considered in the balance-of-plant (BoP) components and SOEC stack designs. A design for high flow rates results in increased capital expenditures and inefficiency at low flow rates, while a design optimised for low flow rates leads to high pressure drops (narrow air channels in SOECs) and inefficiency at high flow rates. A recent study [8] based on high-resolution solar data shows that adjusting the air mass flow alone does not fully prevent violations of temperature gradient limits during highly fluctuating power supply. The study suggests modulating the steam mass flow to control the temperature gradients, which negatively affects the reactant conversion and thus SOEC electrical efficiency.

An alternative approach to achieving highly dynamic operating point changes involves rapidly switching the current on and off, ensuring that the average power consumption matches the target value [9–11]. This control approach, known as pulse-width modulation (PWM) [12], is widely applied in DC–AC inverters, electric motor controls, and light dimming. However, its application has so far been limited to cell- or single-stack-level experiments in laboratory settings, with no demonstrations at system scales relevant to practical applications.

Many control strategies assume that fluctuations in power supply are directly transferred to the SOEC stacks. However, large-scale systems will likely consist of multiple modules [13]. This is the case for the currently largest existing SOEC systems in the range of 2.6 MW_{el} to 4 MW_{el} [14,15]. If a plant is fully designed in a modular way, individual modules can be operated at different operating points [16]. With sufficient modules, fluctuating power supply can be managed by switching the modules' operating point between hot standby and nominal (modular on/off approach), as demonstrated by Tomberg et al. [17]. The authors introduced a strategy for the transition from hot standby to the thermoneutral point, bypassing the endothermic region with a current step, followed by a controlled increase in current to prevent exceeding temperature gradient limits. This strategy prevents inefficient and degradation-prone operations far from the design point. However, the plant's flexibility and the required energy buffer storage (e.g., batteries) strongly depend on the number of modules. Additionally, power is controlled only indirectly by setting the target outlet temperature, which is imprecise, slower and potentially requires iterative adjustments.

This work addresses this limitation by analysing the potential of extending the modular on/off approach to increase flexibility by introducing an operating range around the isothermal, nominal point for

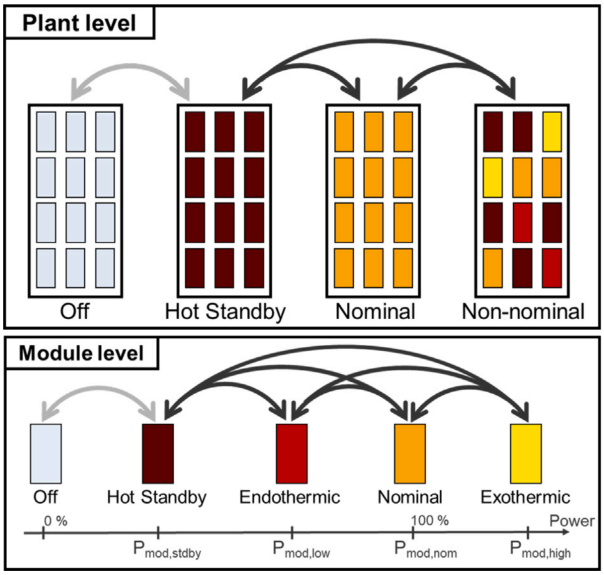

Fig. 1. Schematic illustration of the different operating points on plant and module level. Arrows indicate the relevant changes of operating points that occur in transient operation.

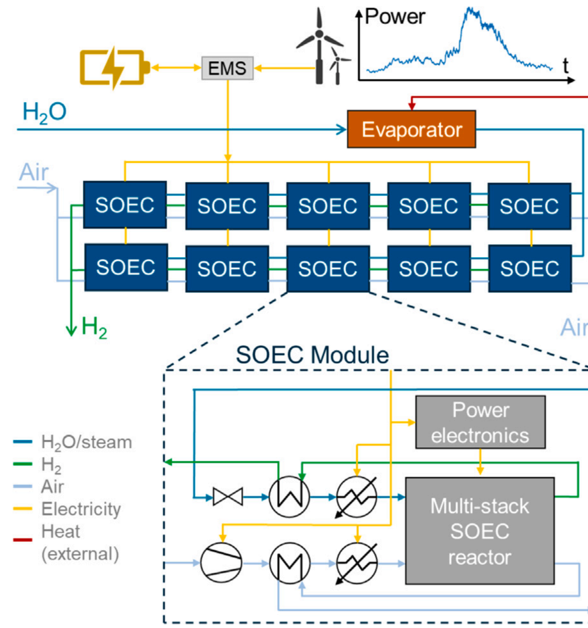

Fig. 2. Modular SOEC plant with renewable energy input. The single module is a sub-system comprising a multi-stack SOEC reactor with heat exchangers, electric heaters and air blower.

each module. Fig. 1 illustrates the possible operating points at both the plant and module levels. At the module level, in addition to the hot standby and nominal operating points (OPs), an extended operating range is defined, spanning from an endothermic point ($P_{\mathrm{mod,low}}$) to an exothermic point ($P_{\mathrm{mod,high}}$). At the plant level, individual modules can operate at different OPs, enabling a more flexible overall plant power consumption.

This study aims to address three key questions regarding the transient operation of modular SOEC systems, specifically:

(i) What is the optimal combination of number of modules and the individual module's operating range for dynamically operated modular plants?
(ii) Can a proposed simple control concept enable safe and rapid transitions within the defined operating range?
(iii) Does this modular control concept prove to be beneficial at the plant level, particularly in terms of transient capability, module count, and required energy buffering capacity?

The desired transient capability and the number of modules at the plant level impose corresponding requirements on individual modules. In turn, the transient performance of a single module dictates the overall transient capability of the plant. To investigate the above mentioned questions while considering the interdependence between plant- and module-level dynamics, the paper is structured as follows:

First, a modular plant layout and the single-module subsystem are presented as the basis for the investigations, together with the applied modelling approach. Next, a theoretical analysis examines the relationship between total plant power, the module operating range, and the number of modules, with a focus on their impact on part-load behaviour. The analysis then shifts to the module level, where a suitable operating range for individual modules is defined. Based on these boundary conditions, a control concept is developed, using power as the set-point, that ensures safe and rapid transitions between all operating points. This approach extends the strategy by Tomberg et al. [17] for transitioning from hot standby to isothermal operation. A sensitivity analysis follows, identifying key control parameters for optimising transition time and efficiency. Finally, the characteristic power profiles of the individual module are applied to a multi-module plant following a real wind power profile. A Python-based power distribution algorithm is introduced, which is used to evaluate how the module operating range and the number of modules influence the plant's ability to follow fluctuations in power supply. The paper concludes with a summary of the main findings.

2. Methodology

2.1. Modular plant layout

For comparability with Tomberg et al.'s results [17], a similar modular plant configuration is adopted, as shown in Fig. 2. The plant comprises a variable number of N identical modules, each consisting of a multi-stack SOEC reactor, power electronics, fuel and air heat exchangers, electric heaters, and an air blower, allowing for independent operation. Steam is assumed to be generated centrally and distributed to each module, where a valve regulates the mass flow. The steam is produced using excess heat from a downstream process, such as methanation, as outlined in Wang et al. [18]. To maintain a generic and end-product-independent analysis, pure steam electrolysis is considered, although co-electrolysis may be advantageous for overall system efficiency depending on the desired end-product. A battery and an energy management system (EMS) balance out the mismatch between fluctuating power supply and the power consumption of the SOEC modules. The primary focus of this study is the transient operation and control concept development for the single SOEC module.

2.2. SOEC module model

The SOEC module was modelled and simulated using TEMPEST [19–22], a Modelica®-based simulation framework developed to analyse the transient characteristics of multi-stack electrochemical reactors within integrated process systems. The model builds upon the subsystem model described in [17], incorporating the same set of components and depicted in the dashed box in Fig. 2. To reduce computational cost, the balance-of-plant components were partially simplified. The fuel and air heat exchangers were replaced with lumped models with a constant effectiveness $\epsilon = \dot{Q}/\dot{Q}_{\max} = 90\,\%$. Variations of this value due to changes in mass flow and fluid properties are neglected, which is justified by the fast response of the electric heater's PID controller. Temperature variations coming from the heat exchangers are compensated by the fast heaters, unless the temperature is already above the setpoint value or available heating power is exceeded. Both does not occur in the simulated conditions. Similarly, heat loss to the environment is neglected for the BoP components, as their impact on the change in inlet temperature at the SOEC is slow and would be compensated by the electric heaters. Therefore, these simplifications have negligible effects on the transient behaviour of the SOEC, although they may lead to slightly underestimated heater power consumption.

The SOEC reactor model itself was adopted unchanged and represents 720 electrolyte-supported cells, arranged into 24 stacks housed within an insulated box, and yielding a total active cell area of $9.20\,\mathrm{m}^2$. The model was previously validated [21] using in-house experiments conducted in the large-scale test environment GALACTICA [23,24], which enables testing of SOC reactors with up to $120\,\mathrm{kW_{el}}$ electrolysis power. The SOEC model is based on a one-dimensional cell model, discretised into five elements in flow direction, providing a detailed representation of activation, ohmic, and diffusion losses, as well as intra-cell and external heat transfer. For each 30-cell stack, a single central cell is modelled in detail, while the remaining cells are represented using a simplification approach [21]. Additionally, heat transfer among stacks and through the insulation is modelled to enable the development of realistic operating strategies for multi-stack reactors, considering transient behaviour and critical parameter distributions like temperature gradients, composition, and current density. Further details on the applied models can be found in [17,21].

Solid oxide cells are sensitive to both spatial and temporal temperature gradients and thereby induced thermal stress [25,26]. The minimum and maximum gradients within the cells are determined by the following equations:

$$\left(\mathrm{d}T_{\mathrm{cell}}/\mathrm{d}t\right)_{\mathrm{min,max}} = \mathrm{min/max}\left(\frac{T^{k,j}_{\mathrm{cell}}(t) - T^{k,j}_{\mathrm{cell}}(t-1)}{\Delta t}\right), \tag{2}$$

$$\left(\mathrm{d}T_{\mathrm{cell}}/\mathrm{d}x\right)_{\mathrm{min,max}} = \mathrm{min/max}\left(\frac{T^{k_{\mathrm{out}},j}_{\mathrm{cell}} - T^{k_{\mathrm{in}},j}_{\mathrm{cell}}}{\Delta x}\right), \tag{3}$$

where T_{cell} is the lumped temperature of the anode, electrolyte and cathode. The indexing k, j represents the kth discretisation element along the flow coordinate within each cell j of the SOEC module. Δx is the length of the equally sized discretisation elements.

2.3. Impact of single module operating range on plant level

In a modular plant the operating point can be adjusted by modifying the operating points of individual modules, with the total plant power defined as $P_{\mathrm{pl}} = \sum_{i=1}^{N} P_{\mathrm{mod},i}$. For generic applicability, both plant and module power P_{pl} and P_{mod} are normalised to their respective nominal values and expressed in percent. To maximise power-following capability, it is essential to minimise gaps in the plant's power range, as these represent unavailable operating points. Exemplary, this is particularly important for renewable-powered electrolysis plants, where closely following fluctuating electricity supply helps reduce curtailment.

When modules operate in an on/off mode – switching between hot standby and nominal operation – the plant power changes in discrete steps, creating gaps in the power range, as shown in the first row of Fig. 3(a): zero module power range P_{mod} = 100–100 % and N=10 modules. The sizes of these gaps depend on the number of modules N, a completely gapless operation would theoretically require an infinite number of modules.

Alternatively, gaps in the plant power operating range can be minimised by allowing each module to operate within a specified range. The minimum achievable steady-state plant power is determined by the lower limit of the module's operating range and the number of modules $P_{\mathrm{pl,min}} = P_{\mathrm{mod,low}}$. $P_{\mathrm{pl,min}}$ corresponds to the lower limit of the first module in each row of Fig. 3(a). The graphic illustrates how

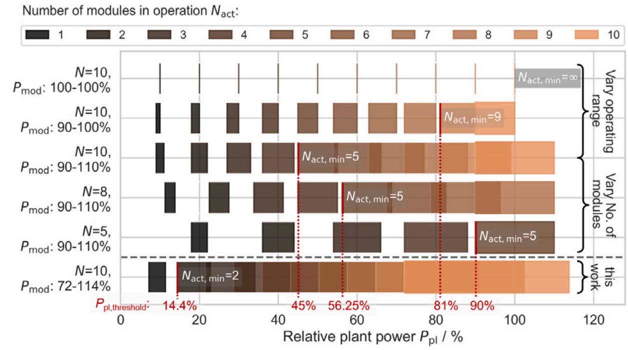

(a) Illustration of the accessible steady-state plant operating ranges (bar segments), as a function of the number of actively operating modules N_{act} (indicated by colour), the total number of modules N and the single module operating range P_{mod} as defined in Eq.(4). Each row along the y-axis to a specific combination of N and P_{mod}.

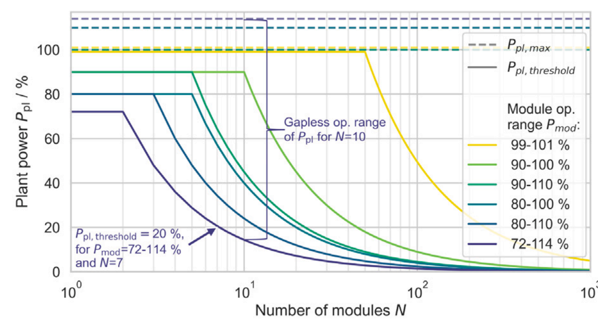

(b) Illustration of the dependency of the threshold plant power $P_{\mathrm{pl,threshold}}$ for gapless operation on the number of modules N (x-axis) and the module operating range P_{mod} (indicated by colour), as defined in Eq. (4). Dashed lines indicate the maximum plant power $P_{\mathrm{pl,max}}$ and solid lines the threshold plant power $P_{\mathrm{pl,threshold}}$. For a given number of modules N, the steady-state gapless operating range corresponds to the vertical range between $P_{\mathrm{pl,max}}$ and $P_{\mathrm{pl,threshold}}$.

Fig. 3. Analysis of the number of modules N and operating range P_{mod} on the plant power according to Eq. (4).

both the variation of the module operating range and the number of modules affect the accessibility of plant power. By comparing the first and second rows, it is evident that introducing a small range of 10 % per module already significantly reduces the gaps and improves the plant's ability to meet a desired power consumption. An increased number of modules operating in active producing (non-hot standby) mode broadens the range of achievable plant power. The threshold plant power, above which gapless operation is possible, can be calculated as:

$$P_{\mathrm{pl,threshold}} = N_{\mathrm{act,min}}\, P_{\mathrm{mod,low}} \propto \left(\frac{P^{\,2}_{\mathrm{mod,low}}}{(P_{\mathrm{mod,high}} - P_{\mathrm{mod,low}})}\right), \tag{4}$$

where $N_{\mathrm{act,min}} = \mathrm{ceil}\left(\frac{P_{\mathrm{mod,low}}}{P_{\mathrm{mod,high}} - P_{\mathrm{mod,low}}}\right) \leq N$ is the minimum number of modules that need to be active in producing operation. The consumption of the modules in hot standby is neglected here. The lower $N_{\mathrm{act,min}}$, the lower $P_{\mathrm{pl,threshold}}$ and the wider the gapless operating range of the plant. Eq. (4) shows that $P_{\mathrm{pl,threshold}}$ is proportional to $P_{\mathrm{mod,low}}$ squared. Thus, $P_{\mathrm{mod,low}}$ is the most effective parameter to reduce the gapless operating range of the plant. The values of $N_{\mathrm{act,min}}$ and $P_{\mathrm{pl,threshold}}$ are provided in Fig. 3(a) as annotated text for each combination of N and P_{mod}. For example, for a module operating range of P_{mod} =72–114 %, gapless operation is achievable with a minimum of $N_{\mathrm{act,min}}$=2 actively operating modules, corresponding to a threshold plant power of $P_{\mathrm{pl,threshold}}$=14.4 %. For a detailed derivation and further analysis of these equations, the reader is referred to the supplementary

Table 1
The operating parameters of hot standby and the Nominal OP (adopted from [17]) as well as the endothermic and exothermic OPs as lower and upper limits of the operating range.

	Hot standby	Nominal OP (Isoth., $P_{mod,nom}$)	Endothermic ($P_{mod,low}$)	Exothermic ($P_{mod,high}$)
Power relative to $P_{mod,nom}$ (incl. power electronics losses)/%	1.79	100	72	113.8
Relative power of BoP (electric heaters and air blower)/%	4.37	5.15	4.58	5.26
Current density/A cm^{-2}	0	0.55	0.40	0.61
Reactant conversion/%	–	70	70	70
$H_2/H_2O/N_2$ inlet molar fractions/%	0.05/0/0.95	0.1/0.9/0	0.1/0.9/0	0.1/0.9/0
O_2 outlet molar concentration/%	21	40	40	40
Air inlet mass flow/g s^{-1} cm^{-2}	2.337×10^{-4}	1.281×10^{-4}	9.346×10^{-5}	1.445×10^{-4}
Forming gas mass flow/g s^{-1} cm^{-2}	3.261×10^{-5}	0	0	0
Module fuel & air inlet temperature/°C	830	830	830	830
Module fuel outlet temperature/°C	802.3	830.5	799	844
Module efficiency (steam production excluded)/kW h kg^{-1}	–	38.64	38.62	38.71

information (SI-1). Fig. 3(b) analyses the dependency of the $P_{pl,threshold}$ for a wide range of the number of modules and further module power operating ranges. The case without an operating range is not shown since $N_{act,min}$ is not defined for $P_{mod,high} = P_{mod,low}$. However, the figure shows that increasing the range from 2 % (yellow) to 10 % (light green), the required number of modules to obtain a $P_{pl,threshold}$ of 20 % reduces from $N = 250$ to $N = 45$. While $P_{mod,high}$ is constrained by limiting cell temperature and voltage, $P_{mod,low}$ could be set to zero, which would lead to a completely gapless operating range with a single module ($N = 1$). However, larger deviations from the isothermal operating point (100 %), lead to larger temperature variations between operating points. In transient operation this increases the risk of too high thermal gradients. Transitioning between these operating points must be executed slowly. Based on these considerations and a plant consisting of N=10 modules, an operating range for the single module is defined in the following subsection.

2.4. Operating range for the single module

The hot standby point and the Nominal OP are adopted from Tomberg et al. [17] for comparability. Building on the previous analysis of the effect of the operating range on the plant power and taking into account temperature limitations, two additional points are defined that span the operating range around the Nominal OP: $P_{mod,low} < P_{mod,nom} < P_{mod,high}$. The four key operating points are defined as follows and summarised in Table 1.

- **Hot Standby** ($P_{mod,stdby}$): Fuel and air inlet temperatures are the same as during operation. The fuel-side composition is changed to forming gas and the air mass flow is set to keep the cell temperatures in a range of ±10 K around 800 °C.
- **Nominal OP** (Isothermal, $P_{mod,nom}$): This is defined as the isothermal point, corresponding to a fixed inlet temperature and mass flow rates, as given in Table 1. For this case, the nominal power is $P_{mod,nom}$= 69 kW, referred to as 100 % power at the power electronics, excluding the contributions from the electric heaters and air blower.
- **Endothermic OP** ($P_{mod,low}$): The lower limit of the operating range is set at 72 % of the nominal power, ensuring gapless operation starting at low plant powers below 20 % (see the last row of Fig. 3(a)). This threshold is chosen to maintain cell temperatures not lower than those in hot standby mode, preventing excessive temperature fluctuations that could impact system longevity. However, lower temperatures can be justified, if the advantages in flexibility outweigh the potential negative impact on lifespan. The optimal balance is a techno-economic decision, depending on the specific use case and the degradation behaviour of the stacks used.
- **Exothermic OP** ($P_{mod,high}$): The upper limit of the range is set at 114 % power, chosen to be as high as possible without exceeding the maximum cell temperature of 850 °C, specified by the SOEC manufacturer. A key limitation of this definition in real systems is the effect of voltage degradation over time, which may be compensated through increasing the operating temperature. However, this reduces the available range before the temperature limit is reached, potentially restricting full use of the defined operating range. In this study, the maximum applicable exothermic point is considered nonetheless, in order to allow for larger temperature differences and thus for more extreme operating point changes.

The module efficiencies in Table 1 show minimal variation across the three active operating points. This is because all variables scale linearly with current: H_2-production due to a 100 % faradaic efficiency, SOEC power due to the ohmic-dominated region, and the electric heater power due to scaled air and fuel flows and a constant heat exchanger effectiveness. The blower power remains negligible at the low flow rates considered.

In highly transient operations, each individual SOEC module must be able to transition safely and rapidly between defined operating points. The following section develops and analyses a control concept tailored to meet these requirements.

3. Transient operation of single module

Contrary to steady-state SOEC operation, which aims to achieve maximum system efficiency and minimum degradation to reduce hydrogen production costs, transient operation introduces challenges related to ensuring operational safety and the module's ability to handle rapid transitions. Beside the generally applicable degradation relevant operating parameters, such as the maximum cell voltage and spatial temperature gradient $\left(\mathrm{d}T_{cell}/\mathrm{d}x\right)_{min,max}$, the temporal temperature gradient $\left(\mathrm{d}T_{cell}/\mathrm{d}t\right)_{min,max}$ is specifically relevant in transient operation and therefore used as the main criterion regarding safe and low degradation operation. The key evaluation criteria applied in this work are:

- Safe and low degradation operation: temporal and spatial temperature gradients, $\left(\mathrm{d}T_{cell}/\mathrm{d}t\right)_{min,max}$, $\left(\mathrm{d}T_{cell}/\mathrm{d}x\right)_{min,max}$
- Efficiency: $\eta = \frac{\dot{n}_{H_2} \cdot LHV_{H_2}}{P_{el,PE}+P_{el,BoP}}$
- Transient capability: transition time between operating points, based on the power set-point P_{set}

3.1. SOEC module control concept

To enable cost-effective commercial deployment, equipping SOEC modules with extensive sensors for measuring intra-cell thermal gradients is impractical. Instead, the proposed approach combines a limited number of representative temperature sensors (T_{TC}) with a validated model. These sensors, located at the air outlet of the centre cell in each stack, provide inputs to standard controllers in a robust control concept.

Tomberg et al. [17] introduced a temperature-controlled strategy that reduced the transition time from hot standby to isothermal operation by a factor of about four compared to conventional linear current

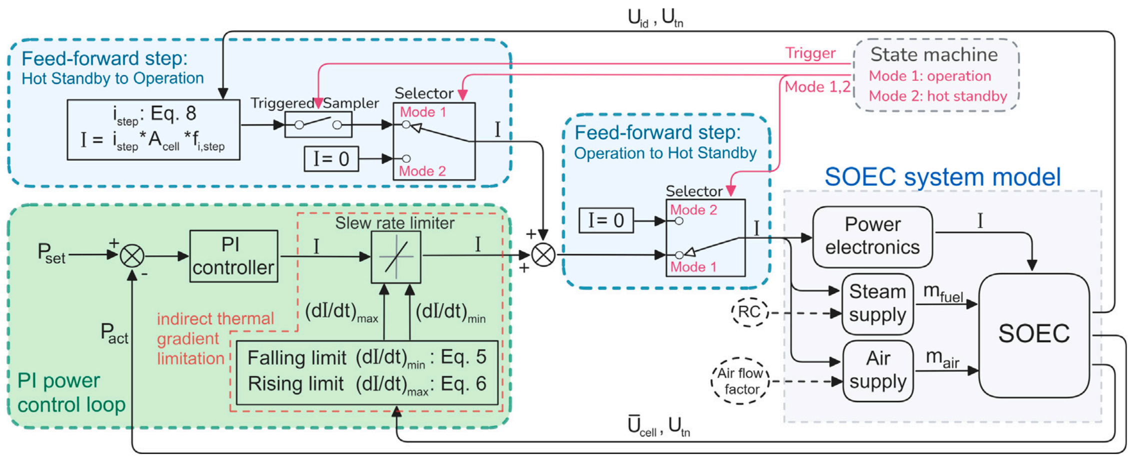

Fig. 4. Schematic overview of the developed SOEC Module Control Concept. The PI power control loop (green) ensures the setpoint power is reached quickly while limiting thermal gradients. Two feed-forward steps (blue) enable rapid transitions between hot standby and active operation. (For interpretation of the references to colour in this figure legend, the reader is referred to the web version of this article.)

ramps. In this work, that strategy is adapted to a power-controlled approach and extended into a control concept capable of handling all required operating point changes, including power modulation around the nominal point. Fig. 4 provides a schematic overview of the proposed control concept. At its core, a proportional–integral (PI) power control loop minimises the error between the set and actual power by adjusting the current. The change rate of the output current is subsequently dynamically constrained by a slew rate limiter, ensuring compliance with defined temperature gradient limits. Additionally, two feed-forward steps minimise transition times: one directly steps to the thermoneutral current when switching from hot standby to operation, whereas the other immediately sets the current to zero when transitioning back to hot standby. Together, these elements ensure fast yet controlled power adjustments while also limiting thermal stress.

PI power control loop

The PI-controller minimises the error between the set and actual power by modulating the current. Its tuning is based on the step-response method and further refined manually for quick convergence with moderate overshoot. Further details are provided in the supplementary information (SI-2). Since the PI-controller is followed by a slew rate limiter, its tuning effectively impacts the applied current when the change rate of the output signal is small. The slew rate limiter constrains the temperature gradients by limiting the rate of current change. The minimum and maximum current change rates are inversely proportional to the difference between the average cell voltage and the thermoneutral voltage, which corresponds to heat generation [17]:

$$(\mathrm{d}I/\mathrm{d}t)_{\min} = -\frac{1}{\max\left(a(\overline{U_{\mathrm{cell}}} - U_{\mathrm{tn}}) + b,\ C_{\min}\right)} \tag{5}$$

$$(\mathrm{d}I/\mathrm{d}t)_{\max} = \frac{1}{\max\left(c(\overline{U_{\mathrm{cell}}} - U_{\mathrm{tn}}) + d,\ C_{\max}\right)} \tag{6}$$

The thermoneutral voltage U_{tn} is calculated according to Eq. (1) with the temperature averaged between the set inlet temperature and the maximum of the measured air outlet temperatures:

$$U_{\mathrm{tn}} = \frac{\Delta^{\mathrm{R}} H_{\mathrm{m}}\left(\frac{1}{2}(T_{\mathrm{in,set}} + T_{\mathrm{stack,max}})\right)}{z(x_{\mathrm{Fuel,in}})\,F} \tag{7}$$

The parameters a, b, c, and d are calibrated based on system-specific thermal gradient limits, which vary depending on cell and stack design. Table 2 lists the parameter values for three selected gradient limits, each carefully tuned to enable rapid transitions without exceeding thermal constraints.

Table 2
Parameters for the minimum and maximum slew rate limits in Eq. (5),(6) for three different temperature gradient limits.

Parameter	Temperature gradient limit $(\mathrm{d}T_{\mathrm{cell}}/\mathrm{d}t)_{\min,\max}$		
	$\pm 2.5\,\mathrm{K\,min^{-1}}$	$\pm 5\,\mathrm{K\,min^{-1}}$	$\pm 10\,\mathrm{K\,min^{-1}}$
a	240	210	36
b	18	1.8	0.6
c	-440	-110	-5
d	13	3.4	0.6

To determine these values, the simulated maximum and minimum temperature gradients were analysed to ensure they consistently reach but do not exceed the respective limits. Regions requiring higher or lower gradients were identified based on $\overline{U_{\mathrm{cell}}} - U_{\mathrm{tn}}$, and the parameters were adjusted accordingly. To streamline tuning and minimise iteration steps, the slew rate limits $(\mathrm{d}T_{\mathrm{cell}}/\mathrm{d}t)_{\min,\max}$ were plotted against $\overline{U_{\mathrm{cell}}} - U_{\mathrm{tn}}$ (cf. Eqs. (5), (6)). This visualisation provided an effective method to evaluate the effects of parameter changes on the curve shapes. Additional plots illustrating the slew rate limits as functions of the voltage difference are available in the supplementary information (SI-2). For this work, the reference thermal gradient limit is set to $\pm 5\,\mathrm{K\,min^{-1}}$, which applies to all results unless otherwise specified.

To address extreme voltage differences that typically occur at the start of a transition, the denominator in the slew rate equations is further limited by a constant value, with $C_{\min} = 1$ and $C_{\max} = 0.1$. It should be noted, that the current in electrolysis mode is defined as negative. Consequently, $(\mathrm{d}I/\mathrm{d}t)_{\max}$ and $(\mathrm{d}I/\mathrm{d}t)_{\min}$ correspond to decreasing and increasing absolute currents, respectively.

Feed-forward steps

Transitions from hot standby to isothermal operation pass through an endothermic region, causing significant cooling effects. Rapid ramp rates can induce large temperature gradients, accelerating stack degradation or premature failure. To mitigate this, slow ramp rates are usually used, accepting longer transition times. However, a direct step to the thermoneutral operating point, based on the hot standby temperature, bypasses the endothermic region, resulting in minimal temperature gradients.

Similarly, for transitions to hot standby, a direct step to 0 A prevents endothermic cooling. Therefore, for changes between hot standby and a producing operating point, two additional steps are introduced, effectively bypassing the PI controller:

1. Hot standby to Operation: When the state machine mode switches from hot standby to operation, the sampler is triggered. This causes the sampler to update its output once and hold that value until the next trigger event. Simultaneously, the selector switches to forward the sampler's output, allowing the current to step directly to thermoneutral operation. The corresponding current density is approximated with Ohm's law [17]:

$$i_{\text{step}} = \frac{U_{\text{id}} - U_{\text{tn}}}{ASR}\text{, with} \tag{8}$$

$$U_{\text{id}} = U_0 + \frac{R\,\frac{1}{2}\left(T_{\text{in,set}} + T_{\text{TC,max}}\right)}{z\,F}\ln\left(\frac{\overline{y_{\text{H}_2}}\;\overline{y_{\text{O}_2}}^{0.5}}{\overline{y_{\text{H}_2\text{O}}}}\left(\frac{p}{p_0}\right)^{0.5}\right),$$

$$ASR = 725\,\Omega\,\text{cm}^2\ \exp(-0.008\,29\,\text{K}^{-1}\ \overline{T_{\text{TC}}}).$$

Where U_{id} is the ideal voltage, $\overline{y_i}$ represents the in- to outlet averaged species concentrations. The total area specific resistance ASR is determined through short-stack experiments by Riedel et al. [27]. Here, it is calculated using the average of the measured air outlet temperatures $\overline{T_{\text{TC}}}$. The experiments can be easily repeated for the case when different stacks are used. After this step, the PI power control loop completes the transition until $P_{\text{set}} = P_{\text{act}}$.

2. Operation to Hot standby: When the state machine mode switches from operation to hot standby, a second selector switches the output value to zero, resulting in an immediate step to zero current.

The combined output of the feed-forward steps and PI power control loop determines the current sent to the power electronics. The air and mass flow setpoints are determined based on the applied current and given RC and outlet oxygen concentration. Air and fuel flows are continuously adjusted, with fuel flow changes timed to avoid starvation or abrupt fluctuations. These processes are managed by the state machine, which also sets the PI controller limits to ensure rapid convergence to a wide range of power set-points.

The proposed control concept, consisting of standard controllers, is straightforward to implement in a module control system. The following subsections analyse its performance across the defined operating range and evaluate its capability to handle dynamic plant operations.

3.2. Transitions between operating points

In order to evaluate the performance of the control concept it is first compared to the temperature-control strategy of Tomberg et al. [17] for the transition from Hot Standby to the Nominal OP. Subsequently, it is tested for the most extreme transitions within the defined operating range, including those with the largest temperature changes and current steps.

3.2.1. Transition from hot standby to the nominal OP

The transition begins with adjusting the fuel mass flow and composition from forming gas to steam, a process assumed to take 30 s throughout the whole study. Immediately afterwards, the feed-forward step increases the current according to Eq. (8), followed by control via the PI power control loop. While in [17] temperature is employed as the control variable, this work uses power instead. Fig. 5 compares the two approaches based on key operating parameters: relative power and current density (the main controlled and manipulated variables, shown in panel a), cell voltage range (panel b), temperature gradient range (panel c), and cell temperature range (panel d). The depicted ranges represent the local variation of each parameter, with the solid lines showing the minimum and maximum values across all discretised cells at each time point. While the temperature-controlled approach reaches the final temperature faster, the power-controlled approach stabilises at the set power faster. Both methods follow a similar current profile, with the initial step corresponding to approximately 60 % of the final steady-state current. The steeper rate of change immediately after the step in the power-controlled case is due to the tuned parameters a and b in Eq. (5), defining the minimum slew rate for the current change in negative direction. Afterwards, both methods display similar current and power profiles, but the power-controlled approach converges after about 3.8 min at 100 % power. In contrast, the temperature-controlled method experiences an overshoot by 7 % and converges after ca. 50 min as the final temperature is achieved. Compared to conventional linear current ramps, satisfying the same temperature gradient limits, the power-controlled approach enables a transition time reduction by a factor of five to six. A detailed comparison is provided in the supplementary information (SI-3).

Throughout the slew rate-limited phase, the applied temperature gradient limit of $\pm 5\,\text{K}\,\text{min}^{-1}$ is maintained. However, immediately after the step, temperature gradient peaks briefly exceed the limit for about three seconds. Despite this short-term violation, the actual temperature change during this period is less than 1 K, resulting in negligible mechanical stress. Experimental tests of rapid current steps have shown no damage to cells under similar conditions [9,28,29]. Consequently, these peaks are considered harmless. Similar short-term peaks observed in subsequent results can be justified following the same rationale. As stated at the beginning of this section, spatial temperature gradients $(\text{d}T_{\text{cell}}/\text{d}x)_{\text{min,max}}$ have to be evaluated as well. These gradients are less sensitive to controller parameters and remain within an uncritical range of $-4\,\text{K}\,\text{cm}^{-1}$ to $2\,\text{K}\,\text{cm}^{-1}$. Their temporal evolution is presented in the supplementary information (SI-4).

3.2.2. Transition to hot standby

The transition to hot standby from any operating point is achieved by stepping directly to 0 A, as motivated in the previous subsection. This method is the fastest possible way and reduces thermal stress compared to linear ramping. An analysis of linear ramps with various ramp rates showed no significant advantages over the direct step-down approach. Detailed results of this analysis are provided in the supplementary information (SI-5). The most extreme step-down from $P_{\text{mod,high}}$ to hot standby is shown in Fig. 6, demonstrating compliance with the $\pm 5\,\text{K}\,\text{min}^{-1}$ limit. The variation in gradients during the first 30 s results from change to hot standby mass flow and composition. Thereafter, the stacks cool down at a moderate minimum gradient.

3.2.3. Extending to the operating range

The developed control concept is tested to manage all extreme transitions within the operating range while adhering to specified thermal gradient limits. These transitions, involving the largest temperature changes and highest potential thermal gradients, occur between the hot standby, the endothermic operating point with the lowest temperatures, and the Exothermic OP with the highest temperatures, in both directions. Fig. 6 depicts the system's behaviour during these transitions, demonstrating that the applied thermal gradient limit of $\pm 5\,\text{K}\,\text{min}^{-1}$ is consistently maintained (shown in panel c). The transition from hot standby to the Exothermic OP (blue) follows the same strategy that is used above for the Isothermal OP, but with a higher power set-point. Changing between the Endothermic and Exothermic OPs (orange and green) is smoothly handled by the slew rate limited PI power control loop, ensuring controlled and safe changes. Meanwhile, the transition from the Exothermic OP back to hot standby (red) is managed by a feed-forward step, which allows for a rapid and precise power reduction. These results proof the robustness and adaptability of the control concept, which reliably handles even the most extreme transitions within the operating range without exceeding temperature gradient limits.

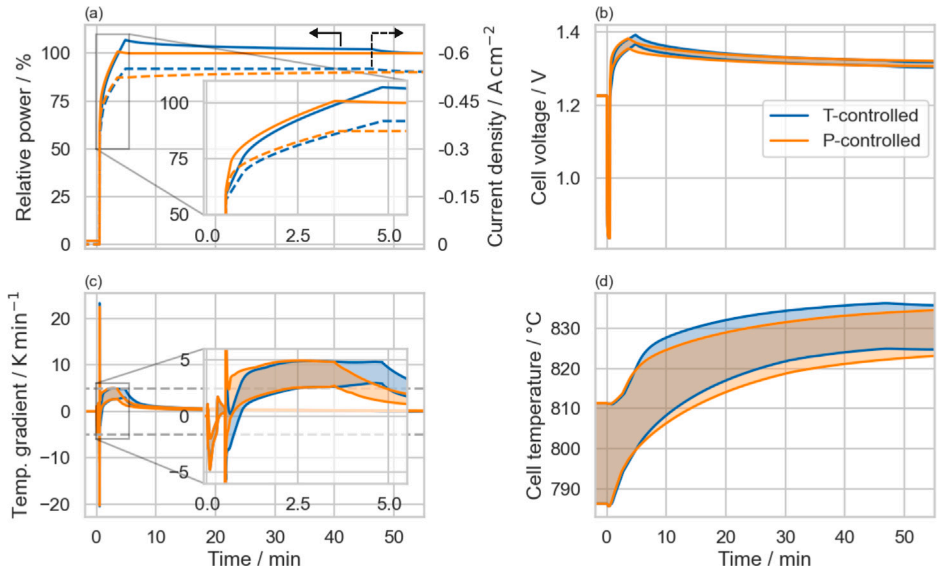

Fig. 5. Comparison of the temperature-controlled (blue) and the power-controlled (orange) transition from hot standby to the Nominal OP in terms of the profiles of relevant operating parameters. (For interpretation of the references to colour in this figure legend, the reader is referred to the web version of this article.)

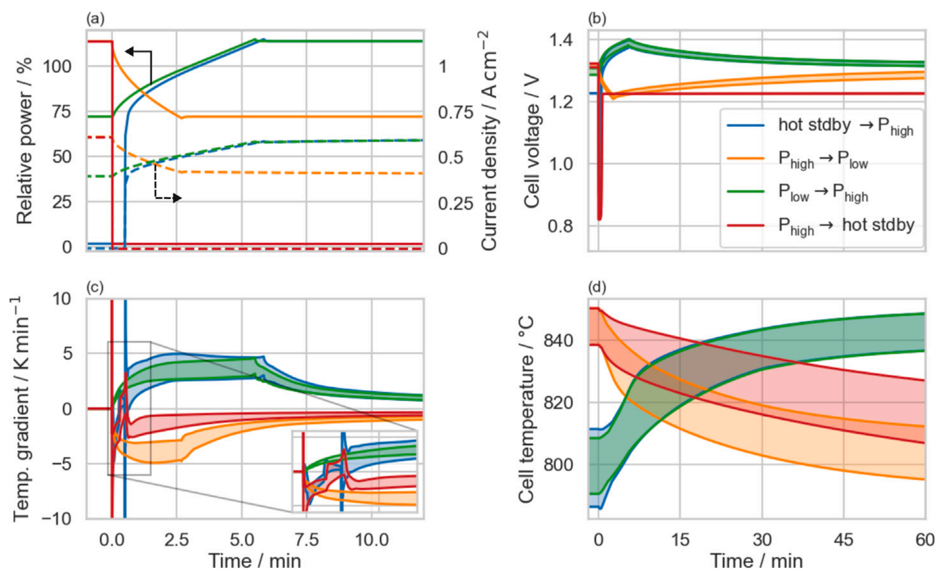

Fig. 6. Application of the control concept for the most extreme switches within the operating range and hot standby. The behaviour of the most relevant operating parameters is shown. (For interpretation of the references to colour in this figure legend, the reader is referred to the web version of this article.)

3.3. Sensitivity analysis

To further optimise system performance, a sensitivity analysis is conducted, focusing on two key metrics: transition time and module efficiency during transitions. The transition time is defined as the period from initiation to when the absolute power difference is below 1 %, $|P_{set} - P_{act}| \leq 1\%$. The efficiency during the transition is evaluated as the LHV-based efficiency, integrated over a fixed 10 min period for comparability:

$$\bar{\eta} = \int_{t=0}^{t=10\,min} \frac{\dot{n}_{\mathrm{H_2}}(t) \cdot LHV_{\mathrm{H_2}}}{P_{\mathrm{el,PE}}(t) + P_{\mathrm{el,BoP}}(t)} \mathrm{d}t \tag{9}$$

The following four parameters are analysed:

- Current step factor $f_{\mathrm{i_{step}}}$ in: $i_{\mathrm{step}} = \left(U_{\mathrm{id}} - U_{\mathrm{tn}}\right)/ASR \cdot f_{\mathrm{i_{step}}}$
- Air mass flow factor $f_{\mathrm{m_f,air}}$ in: $\dot{m}_{\mathrm{air}} = \dot{m}_{\mathrm{air,ref}} \cdot f_{\mathrm{m_f,air}}$
- Reactant conversion: $RC = \frac{I\, n_{\mathrm{cells}}\, M_{\mathrm{fuel}}}{z_{\mathrm{fuel}}\, F\, \dot{m}_{\mathrm{fuel}}}$
- Temperature gradient limit $(\mathrm{d}T_{\mathrm{cell}}/\mathrm{d}t)_{\mathrm{min,max}}$ indirectly controlled via parameters a, b, c and d according to Table 2.

The reference case uses $f_{\mathrm{i_{step}}}$ =1, $f_{\mathrm{m_f,air}}$ =1, RC =70 % and $(\mathrm{d}T_{\mathrm{cell}}/\mathrm{d}t)_{\mathrm{min,max}}$ =±5 K min^{-1}. The reference $\dot{m}_{\mathrm{air,ref}}$ during the transition is the hot standby value given in Table 1. The ranges for parameter variations were chosen based on practical considerations: Lower RC values lead to less efficient use of steam, while higher values close to 100 % can cause local fuel starvation and faster degradation, thus a range of 50 %–90 % is considered. The airflow rate can be reduced to zero, producing pure oxygen – a concept with significant design advantages that several stack manufacturers are exploring. However, due to the associated material and safety challenges, it is not yet considered state-of-the-art. Consequently, the smallest air mass flow factor considered is 0.2, leading to a maximum oxygen concentration of 60 mol %. Increasing air flow rates increases the blower power consumption and is therefore limited to a factor of 5 times the reference flow rate. Both, air mass flow

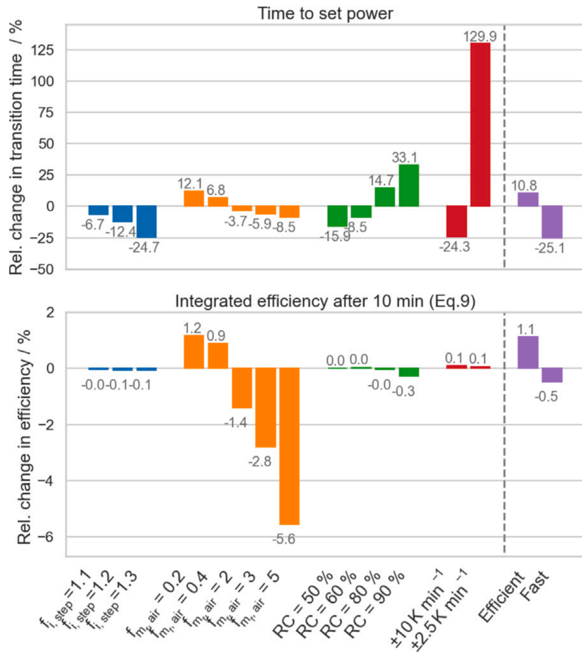

Fig. 7. Transition from hot standby to Nominal OP: Summary of the relative changes (to reference set) in the transition time and the integrated efficiency after 10 min for all parameter variations as well as for the efficient and fast parameter sets.

factor and RC are set to the reference values when the set-point power is reached. Figures showing the effects of the parameter variations on the profiles of relevant operating parameters are available in the supplementary information (SI-4). Fig. 7 summarises the effects of parameter variations on transition time and efficiency. The temperature gradient limit has the strongest influence on transition time, followed by reactant conversion, while air mass flow plays a minor role. In contrast, the impact of these variations on efficiency is generally lower, with only air mass flow exhibiting a significant effect.

Reducing transition time enables faster changes between operating points, thus allowing for faster adjustments in power consumption at the plant level. Doubling the temperature gradient limit reduces transition time by 24 %, whereas halving it results in a 130 % increase due to the nonlinear relationship between current and Joule heating ($\dot{Q} \propto I^2 R$). At higher currents, the rate of heat generation increases more significantly, requiring a slower rate of current change to prevent excessive heating. Besides the temperature gradient limits, current step factor $f_{i_{step}}$ and RC offered the greatest potential for improvement. Adjusting the current step is equivalent to using different temperatures to determine the voltage and ASR values in Eq. (8). As a result, the step does not achieve thermoneutral operation but instead leads to slightly exothermic operation with increased thermal gradients (see Fig. 8). Varying RC affects the cell voltage, mimicking changes in the minimum slew rate, as the latter is a function of the cell voltage.

Regarding efficiency, air mass flow showed the strongest influence, with a potential efficiency gain of 1.2 % at 20 % of the reference flow rate ($f_{m_f,air}$=0.2). Higher flow rates for $f_{m_f,air} > 1$ significantly reduced efficiency, while having only a minor positive effect on transition time.

Relevant parameter profiles of a selection of the parameter variations are shown in Fig. 8. The variation of $f_{i_{step}}$ reveals that a factor of 1.3 violates the $\pm 5\,\mathrm{K\,min^{-1}}$ limit (see panel c) due to excessively exothermic operation caused by the increased step size. For $f_{i_{step}}$ =1.2, the gradients remain well within the limits, while the time reduction is only half compared to $f_{i_{step}}$ =1.3. For all cases, except $f_{i_{step}}$ =1.3 and $f_{m_f,air}$=5, the respective temperature gradient limits are satisfied. Furthermore, the results confirm that the control concept is robust and capable of handling different temperature gradient limits by adjusting parameters a, b, c and d, as outlined in Table 2.

Similar trends are observed for transitions between endothermic and exothermic operating points in both directions. Results for all parameter variations are provided in the supplementary information (S-4).

The insights from the sensitivity analysis are used to improve the transition, aiming for reduced transition time and increased efficiency. Setting each parameter to the value with maximum time reduction or efficiency gain would violate the temperature gradient limit. Therefore, moderate values are identified for two parameter sets – Fast and Efficient – that satisfy the $\pm 5\,\mathrm{K\,min^{-1}}$ gradient limit:

- **Reference:** $f_{i_{step}}$ =1, RC =70 %, $f_{m_f,air}$ =1
- **Fast:** $f_{i_{step}}$=1.25, RC =65 %, $f_{m_f,air}$ =1.5
- **Efficient:** $f_{i_{step}}$ =1.1, RC =70 %, $f_{m_f,air}$ =0.2

In the Fast parameter set, $f_{i_{step}}$ is the dominant factor. The combination of a lower RC and higher air flow would otherwise lead to excessive thermal gradients, so these values were moderately adjusted. For the Efficient parameter set, $f_{m_f,air}$ is the key factor, as it is the parameter with strongest influence on efficiency. To offset the increased transition time caused by reduced air flow, $f_{i_{step}}$ is slightly increased. RC has minimal influence on efficiency but would play a larger role if the evaporation energy of steam were also considered. The effects of these parameter sets on transition time and efficiency are illustrated in Fig. 7, to the right of the dashed line. Efficiency gains are achieved by reducing the air flow, improving efficiency by 1 percentage point, from 82.23 % to 83.15 %. The Fast parameter set reduces the transition time by approximately 25 %, from 3.8 min to 2.85 min. This reduction is comparable to the improvement achieved with a doubled temperature gradient limit of $\pm 10\,\mathrm{K\,min^{-1}}$, while the associated efficiency loss remains negligible. This reveals that the control parameters inherit significant potential to improve the transition time and thus the dynamic behaviour of the SOEC system. By applying an optimisation method, the improvements can be maximised for a specific system with its specific components.

4. Transient operation of a multi-module plant

Building on the developed control approach for a single module, its application in a multi-module plant under transient operation is investigated. A realistic fluctuating power supply is simulated using a power profile from a wind park with 12 turbines [30]. It is explored how the operating range P_{mod} and the number of modules N influence the plant's ability to dynamically match its total power consumption with the supplied power.

For that purpose, a power distribution algorithm with variable $P_{mod,low}$, $P_{mod,high}$ and N is implemented and executed in Python. The key dynamic power characteristics for the extreme transitions, as described in Section 3.2.3, are exported as look-up tables to model power changes over time for individual modules. The algorithm minimises the mismatch between supplied and consumed power, assuming any residual mismatch is buffered by an idealised battery with unlimited capacity. This allows for a battery-independent analysis. To optimise power adjustments the required total plant power change ΔP_{pl} is evenly distributed among the active modules, for three reasons: First, this avoids unnecessary transitions between hot standby and producing operation, requiring extra time for fuel mass flow and composition adjustments. Second, for a small number of modules, switching from hot standby to active operation can cause large power changes of P_{pl}, potentially leading to over- or undershooting the set-point. Third, distributing ΔP_{pl} across more modules allows to parallelise and thus accelerate the adjustment of P_{pl}. A module transitions between hot standby and production only if the required power adjustment exceeds

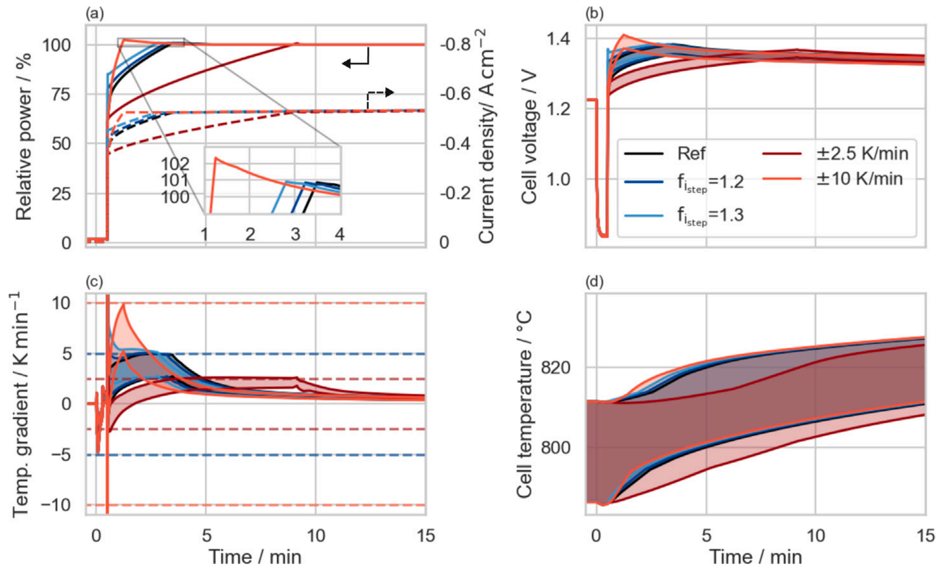

Fig. 8. Results for the changed parameters with the strongest effect on the transient behaviour and the thermal gradients, i.e. $f_{i_{step}}$ and the parameters a and b that determine the temperature gradient limits (see Table 2). The reference case is with $f_{i_{step}}$=1 and a,b for ±5 K min^{-1}.

50 % of $P_{mod,low}$, prioritising the modules based on the First-In, First-Out (FIFO) principle [31]. For all module set-point adjustments, the power profile depends only on the module's initial power. Power changes are interpolated from the look-up table with one-second time steps until the target power is reached. This simplification does not account for temperature-dependent power profiles when modules are not in steady-state after prior transitions. However, it is assumed that these profiles remain valid for reduced operating ranges where limits are within the 72 %–114 % range. More details on the algorithm are provided in the supplementary information (SI-6).

The results are presented in Fig. 9. Plots (a) and (c) show the effects of varying the operating range P_{mod} for a fixed number of modules N =10, while plots (b) and (d) examine variations in N for a fixed P_{mod} =72 %–114 %. The upper plots in (a) and (b) show the supplied wind power P_{wind} (blue) and the total plant power P_{pl} (red to orange) normalised to $P_{pl,nom}$. Below each plot, heat maps depict module operating point changes over time for a fixed P_{mod} =72 %–114 % and fixed N =2, respectively. The boxplots in (c) and (d) quantify the power-following capability for the analysed 60 min period in terms of normalised power mismatch $\left(P_{wind} - P_{pl}\right)/P_{pl,nom}$ in a 1 s-resolution. The boxes represent 50 % of the data points, whiskers extend to the farthest point within 1.5 x IQR (Inter-Quartile Range) [32] and the orange lines indicate the medians. Below, arithmetic means (green) and root mean square errors (RMSEs, magenta) are provided as percentages of $P_{pl,nom}$. Following observations can be made:

- **Effect of operating range** Fig. 9(c): Increasing the operating range significantly reduces the power mismatch $\left(P_{wind} - P_{pl}\right)$, as reflected in narrower whiskers (covering > 90 % of data points), lower values of medians, means and RMSEs. The largest relative improvement occurs when introducing an operating range of 90 %–100 %, compared to the modular on/off approach (P_{mod} = 100 %–100 %). Lowering $P_{mod,low}$ by 10 % yields greater reductions in mean and RMSE values compared to raising $P_{mod,high}$ by the same amount. This aligns with theoretical predictions from Section 2.3, where the threshold power was found proportional to P_{low}^{2}.
- **Effect of Number of modules** Fig. 9(d): For P_{mod} = 72 %–114 %, varying N affects power-following capability particularly at low N. Increasing N by 50 % from 2 to 3 reduces whisker extent and RMSE by approximately a half. Conversely, doubling N from 10 to 20 yields smaller improvements, with whiskers and RMSE reducing by about 27 % and 6 %, respectively. The predominantly negative power differences for small N result from the definition of the power distribution algorithm as applied to precisely this power profile with a large share of small power values.

A sensitivity analysis explores the impact of the two key parameters N and P_{mod} on the plant's power-following capability. The operating range P_{mod} is varied by adjusting $P_{mod,low}$ from 70 % to 100 % in 5 % increments, while keeping $P_{mod,high}$ fixed at 100 %. The module count N is varied from 1 to 15 in single-unit steps. The RMSE of the normalised power difference, $\left(P_{wind} - P_{pl}\right)/P_{pl,nom}$, is used as a measure of the plant's power-following capability, which is visualised as a heat map in Fig. 10. Results for N > 10 are omitted since the RMSE shows little change beyond this point. The trends observed in Figs. 9 are corroborated here. For a fixed $P_{mod,low}$, the RMSE increases moderately as N decreases from 10 to 4, but rises sharply for fewer modules, highlighting the plant's diminishing ability to follow power fluctuations at low module counts. Similarly, reducing $P_{mod,low}$ consistently lowers the RMSE, indicating improved power-following capability. An illustrative iso-RMSE contour line of 5 in Fig. 10 demonstrates the interplay between the operating range and the number of modules. Introducing an operating range of 70 %–100 % at a fixed N = 9, the RMSE reduces by approximately 45 %, from 5.02 to 2.78. This indicates a strong reduction in the average and peak power differences, which in turn reduces the required battery capacity. Alternatively, the number of modules N can be scaled down from 9 to 3 without sacrificing power-following capability, as the RMSE remains close to five.

In summary, expanding the operating range and increasing the number of modules both enhance the plant's ability to follow fluctuating power profiles. The most significant improvements occur when first introducing operating ranges and at lower module counts. Smaller plants, e.g. at smaller wind parks, are more likely to have fewer modules and introducing even a modest operating range allows for cost reductions by decreasing the required module count while maintaining or enhancing performance.

Further improvements in the power-following capability can be realised by addressing certain operational assumptions and refining the algorithm. The time for adjusting the fuel mass flow from forming gas to steam is assumed to be 30 s. Further reducing this time reduces power mismatch during periods of rapid power increases. Using the fast

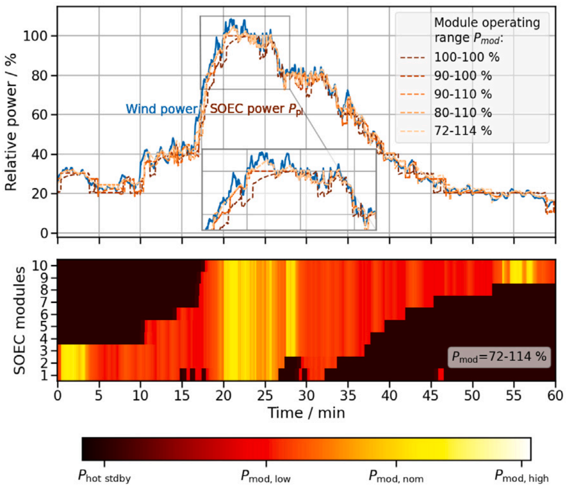

(a) Variation of the operating range while the number of modules is fixed to N=10. *Top*: profiles of the SOEC plant power P_{pl} (red-orange) and the wind power profile (blue). *Bottom*: For an operating range of 72 %–114 %, the change of operating points over time for each module is represented as heat map.

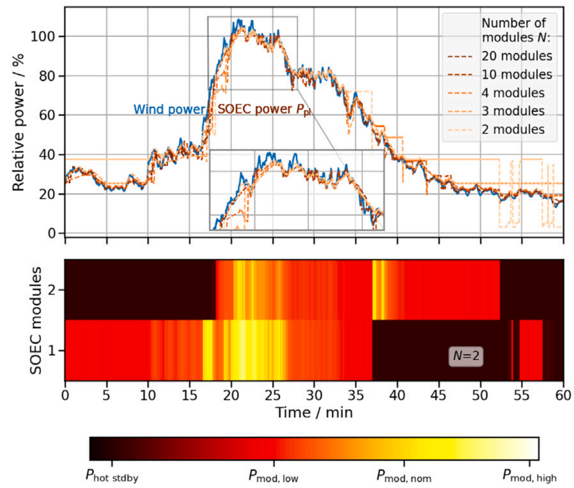

(b) Variation of the number of modules while the operating range is fixed to 72 %–114 %. *Top*: profiles of the SOEC plant power P_{pl} (red-orange) and the wind power profile (blue). *Bottom*: For a fixed operating range 72 %–114 %, the change of operating points over time for N=2 modules is represented as heat map.

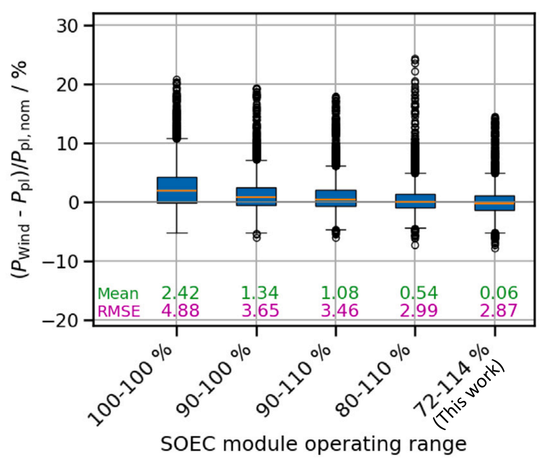

(c) Boxplot of the power differences for the varied operating ranges, while the number of modules is constant at N =10.

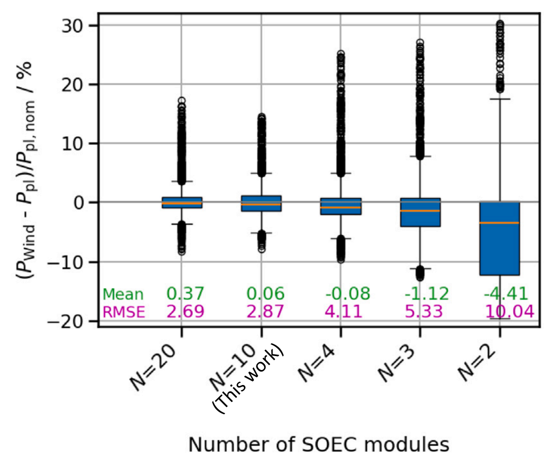

(d) Boxplot of the power differences for the varied number of modules, while the operating range is constant at 72 %–114 %.

Fig. 9. Application of the modular control concept on a multi-module plant with fluctuating wind power supply for varied operating range (left) and number of modules (right). The boxes in the boxplots represent 50 % of the data points, the whiskers extend to the farthest point within 1.5 x IQR (Inter-Quartile Range). (For interpretation of the references to colour in this figure legend, the reader is referred to the web version of this article.)

parameter set from Section 3.3 instead of the reference set could reduce the time to adjust to new power set-points, enhancing responsiveness. The current strategy to switch modules between hot standby and operation follows a First In, First Out approach. A more sophisticated strategy that considers module temperatures and operating histories, e.g. prioritising modules with temperatures closer to the target operating point, could further reduce transition times.

5. Conclusion and outlook

This study explored operating strategies for SOEC reactors, implemented into a control concept and designed to promote highly transient operation in modular plants. Key findings and developments from this work are summarised as follows:

- Correlation for Gapless Multi-Module Plant Operation: A correlation was developed to quantify the impact of the number of modules and their operating ranges on achieving gapless steady-state operation above a threshold plant power. This provides the theoretical foundation for identifying the optimal combination of module range and module count in SOEC plants under dynamic power input scenarios.
- SOEC Module Control Concept: A control approach was proposed for individual SOEC modules, incorporating slew-rate-limited PI control, complemented by feed-forward step changes for transitioning to and from hot standby mode. This approach enables transitions five to six times faster than those achieved with conventional linear current ramps. The analysis of the most extreme transitions demonstrated that this control concept enables fast responses to power fluctuations while effectively limiting thermal stress on the cells.
- Slew Rate Tuning Methodology: A model-in-the-loop methodology for tuning the slew rate of applied electrical current in the PI control loop was demonstrated. This approach successfully constrains temporal temperature gradients within the SOEC stacks using limited temperature measurement data. The control concept relies on standard controllers, which, in contrast to more sophisticated approaches (e.g., Model Predictive Control), are easy to implement and require little computational effort. Coupled with

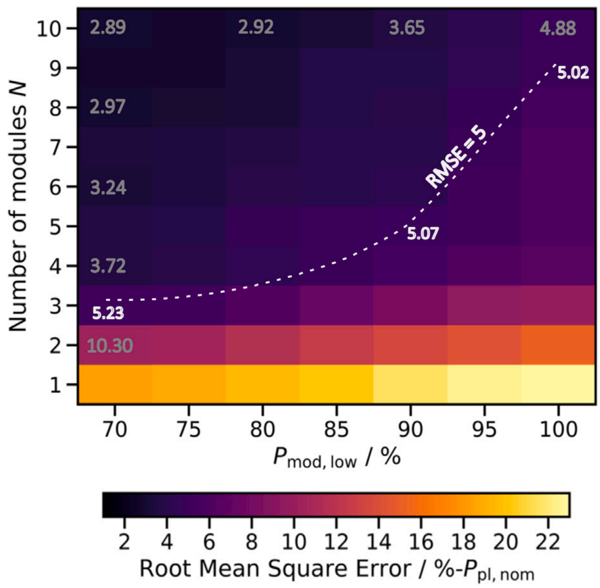

Fig. 10. Root mean square error (RMSE) of the relative power difference (P_{Wind} - P_{pl})/$P_{pl,nom}$ represented as heat map. The number of modules N and the single module's operating range $P_{mod,low}$ - $P_{mod,high}$ are varied, while $P_{mod,high}$=100 %=const.

the straightforward tuning methodology, this approach is both cost-effective and easily adaptable to other systems.

- Control Parameter Tuning Trade-offs: A sensitivity study on the most relevant control parameters quantifies the trade-off between transition speed and efficiency when changing operating points. A parameter set with a moderate temperature gradient limit and optimised for fast transitioning, achieved 80 % of nominal power within 35 s from hot standby, including fuel composition and mass flow adjustments. Full nominal power (100 %) was reached in under three minutes – yielding the same time reduction as doubling the admissible temperature gradient limit. However, efforts to improve integrated efficiency during transitions showed only marginal gains, primarily through a reduction in air flow.
- Multi-Module Plant Performance: A power distribution algorithm was developed to examine the power-following capability of a multi-module plant under a realistic wind park power profile, extending the steady-state correlation from the first bullet point to transient operation. The analysis demonstrates that introducing module-specific operating ranges allows to reduce the module count from 9 to 3 without sacrificing power-following capability. Maintaining the module count the Root-Mean-Square-Error of the power mismatch is lowered by 45 %, enhancing the power-following capability. This, in turn, reduces the required energy buffering capacity, highlighting the operational and design advantages of modular plants with optimised operating ranges.

The presented SOEC module control concept allows for fast changes of the module's operating point and at the same time to maintain operation within prescribed limits, ensuring system durability and performance. On the plant level it enables direct coupling of SOEC plants to highly fluctuating renewable power sources while reducing the dependency on installed battery capacity.

Future work should focus on validating the proposed module control concept in a module-scale hardware-in-the-loop laboratory environment to ensure real-world applicability and robustness. Further, the control concept should be tested in co-electrolysis operation, for which the parameters most likely need different tuning. To avoid the costs and complications associated with placing temperature sensors inside the reactor at each stack, it should be investigated if the reactor outlet temperature could serve as a single measurement point. For an actual application, the power distribution algorithm would need to be optimised, considering the actual and target temperatures of the modules as well as the battery state of charge.

CRediT authorship contribution statement

René Lorenz: Writing – review & editing, Writing – original draft, Visualization, Software, Project administration, Methodology, Investigation, Data curation, Conceptualization. **Jan Hollmann:** Writing – review & editing, Methodology, Conceptualization. **Marius Tomberg:** Writing – review & editing, Methodology, Funding acquisition, Conceptualization. **Marc P. Heddrich:** Writing – review & editing, Validation, Supervision, Project administration, Methodology, Funding acquisition, Conceptualization. **S. Asif Ansar:** Writing – review & editing, Funding acquisition.

Declaration of Generative AI and AI-assisted technologies in the writing process

During the preparation of this work the authors used OpenAI's ChatGPT for assistance with editing and refining of the original manuscript in terms of language, conciseness and structure. After using this tool, the authors reviewed and edited the content as needed and take full responsibility for the content of the published article.

Declaration of competing interest

The authors declare that they have no known competing financial interests or personal relationships that could have appeared to influence the work reported in this paper.

Acknowledgements

This work was financially supported by the German Federal Ministry of Education and Research under grant number 03HY302F and under grant number 03HY116B. The responsibility for the contents lies with the authors.

Appendix A. Supplementary data

Supplementary material related to this article can be found online at https://doi.org/10.1016/j.ecmx.2025.101236.

Data availability

The code of the Modelica library TEMPEST is currently not publicly available. The models used are described in Section 2.2, with further details provided in the cited literature. The wind park power data used in Section 4 and shown in Fig. 9 is available in http://uni-oldenburg.de/fileadmin/user_upload/physik/ag/twist/Forschung/Daten/AnvariEtAl2016_ExampleData _WindPowerAndIrradianceData.zip, accessed June 2022. The power distribution algorithm developed and applied in Section 4 is presented in the supplementary information (SI-6).

References

[1] Buttler A, Spliethoff H. Current status of water electrolysis for energy storage, grid balancing and sector coupling via power-to-gas and power-to-liquids: A review. Renew Sustain Energy Rev 2018;82:2440–54.

[2] Jensen S, Langnickel H, Hintzen N, Chen M, Sun X, Hauch A, et al. Reversible operation of a pressurized solid oxide cell stack using carbonaceous gases. J Energy Storage 2019;22:106–15.

[3] Joule JP. XXXVIII. On the heat evolved by metallic conductors of electricity, and in the cells of a battery during electrolysis. Lond Edinb Dublin Philos Mag J Sci 1841;19(124):260–77.

[4] Cai Q, Adjiman CS, Brandon NP. Optimal control strategies for hydrogen production when coupling solid oxide electrolysers with intermittent renewable energies. J Power Sources 2014;268:212–24.
[5] Saeedmanesh A, Colombo P, McLarty D, Brouwer J. Dynamic behavior of a solid oxide steam electrolyzer system using transient photovoltaic generated power for renewable hydrogen production. J Electrochem Energy Convers Storage 2019;16(4):041008.
[6] Wang Y, Banerjee A, Deutschmann O. Dynamic behavior and control strategy study of CO2/H2O co-electrolysis in solid oxide electrolysis cells. J Power Sources 2019;412:255–64.
[7] Mottaghizadeh P, Fardadi M, Jabbari F, Brouwer J. Dynamics and control of a thermally self-sustaining energy storage system using integrated solid oxide cells for an islanded building. Int J Hydrog Energy 2021;46(49):24891–908.
[8] Liang Z, Chen S, Ni M, Wang J, Li M. A novel control strategy to neutralize internal heat source within solid oxide electrolysis cell (SOEC) under variable solar power conditions. Appl Energy 2024;371:123669.
[9] Schefold J, Brisse A, Surrey A, Walter C. 80,000 current on/off cycles in a one year long steam electrolysis test with a solid oxide cell. Int J Hydrog Energy 2020;45(8):5143–54.
[10] Micero A, Surrey A, Schefold J, Léon A. Fast dynamic electrolysis operation of a 30-cell solid oxide stack. In: 16th European SOFC & SOE forum. Lucerne, Switzerland; 2024, A1501.
[11] Kane N, Hartvigsen J, Shigrekar A, Lambrechtsen J, Olowu T, Casteel M. Dynamic operation of solid oxide electrolysis. In: 16th European SOFC & SOE forum. Lucerne, Switzerland; 2024, A0901.
[12] Storey N. Electronics: A systems approach. 4th ed.. Harlow, England: Pearson Education Limited; 2009.
[13] Lange H, Klose A, Beisswenger L, Erdmann D, Urbas L. Modularization approach for large-scale electrolysis systems: a review. Sustain Energy Fuels 2024;8:1208–24.
[14] Sunfire SE. Press release. 2023, https://sunfire.de/en/news/renewable-hydrogen-project-multiplhy-worlds-largest-high-temperature-electrolyzer. [Accessed 04 March 2025].
[15] Bloom Energy. Press release. 2023, https://investor.bloomenergy.com/press-releases/press-release-details/2023/Bloom-Energy-Demonstrates-Hydrogen-Production-with-the-Worlds-Largest-and-Most-Efficient-Solid-Oxide-Electrolyzer/default.aspx. [Accessed 04 March 2025].
[16] Petipas F, Brisse A, Bouallou C. Modelled behaviour of a high temperature electrolyser system coupled with a solar farm. Chem Eng Trans 2015;45:1015–20.
[17] Tomberg M, Heddrich MP, Ansar SA, Friedrich KA. Operation strategies for a flexible megawatt scale electrolysis system for synthesis gas and hydrogen production with direct air capture of carbon dioxide. Sustain Energy Fuels 2023;7(2):471–84.
[18] Wang L, Chen M, Küngas R, Lin T-E, Diethelm S, Maréchal F, et al. Power-to-fuels via solid-oxide electrolyzer: Operating window and techno-economics. Renew Sustain Energy Rev 2019;110:174–87.
[19] German Aerospace Center (DLR). TEMPEST. 2025, https://www.dlr.de/en/tt/research-transfer/research-infrastructure/modelling-tools/tempest. [Accessed 04 March 2025].
[20] Srikanth S, Heddrich M, Gupta S, Friedrich K. Transient reversible solid oxide cell reactor operation–experimentally validated modeling and analysis. Appl Energy 2018;232:473–88.
[21] Tomberg M, Heddrich MP, Sedeqi F, Ullmer D, Ansar SA, Friedrich KA. A new approach to modeling solid oxide cell reactors with multiple stacks for process system simulation. J Electrochem Soc 2022;169(5):054530.
[22] Sedeqi F, Santhanam S, Riegraf M, Riedel M, Heddrich M, Ansar S. Solid oxide cell reactor model for transient and stationary electrochemical H2O and CO2 conversion process studies. J Electrochem Soc 2024;171(7):074507.
[23] German Aerospace Center (DLR). GALACTICA. 2025, https://www.dlr.de/en/tt/research-transfer/research-infrastructure/test-facilities/galactica. [Accessed 04 March 2025].
[24] Amaya Dueñas DM, Ullmer D, Riedel M, Ventura SS, Metten M, Tomberg M, et al. Performance assessment of a 25 kw solid oxide cell module for hydrogen production and power generation. Int J Hydrog Energy 2024;59:570–81.
[25] Atkinson A, Selçuk A. Mechanical behaviour of ceramic oxygen ion-conducting membranes. Solid State Ion 2000;134(1):59–66, Festschrift dedicated to Prof. Brian Steele.
[26] Botta G, Romeo M, Fernandes A, Trabucchi S, Aravind P. Dynamic modeling of reversible solid oxide cell stack and control strategy development. Energy Convers Manage 2019;185:636–53.
[27] Riedel M, Heddrich M, Ansar A, Fang Q, Blum L, Friedrich K. Pressurized operation of solid oxide electrolysis stacks: An experimental comparison of the performance of 10-layer stacks with fuel electrode and electrolyte supported cell concepts. J Power Sources 2020;475:228682.
[28] Skafte TL, Rizvandi OB, Smitshuysen AL, Frandsen HL, Høgh JVT, Hauch A, et al. Electrothermally balanced operation of solid oxide electrolysis cells. J Power Sources 2022;523:231040.
[29] Kane N, Hartvigsen J, Casteel M, Priest C, Gomez J, Wang L, et al. Accelerated stress testing of standard solid oxide electrolysis cells. ECS Trans 2023;111(6):2139.
[30] Anvari M, Lohmann G, Wächter M, Milan P, Lorenz E, Heinemann D, et al. Short term fluctuations of wind and solar power systems. New J Phys 2016;18(6):063027.
[31] Lange H, Klose A, Lippmann W, Urbas L. Technical evaluation of the flexibility of water electrolysis systems to increase energy flexibility: A review. Int J Hydrog Energy 2023;48(42):15771–83.
[32] Hunter J, Dale D, Firing E, Droettboom M. Matplotlib.Pyplot.Boxplot. 2025, https://matplotlib.org/stable/api/_as_gen/matplotlib.pyplot.boxplot.html. [Accessed 04 March 2025].